Supporting Information

for

Ultralocalized thermal reactions in subnanoliter droplets-in-air

Numerical simulation:

The temperature of the droplet was determined by a systematic and self-consistent numerical solution of coupled electrical and thermal responses of droplet. The details are described below.

Calculation of electric field distribution by electrostatic simulation:

In order to calculate the heating of the droplet, we must first calculate the power-dissipation, $P = 1/2\sigma E_{ac}^2$, at every point within the droplet, see Eqs. 9, 10. The electric field E_{ac} is obtained by solving the Poisson equation (Eq. 1) numerically for the device shown in Supplementary Fig. 5 by using a well calibrated commercial device simulator [1]. Due to high frequency of applied ac bias ($10\ MHz$), the electrostatic screening due to the ac field may be neglected [2], hence ρ is set to zero in the RHS of Eq. S3. Finally, the source and drain are grounded; therefore we assume the channel potential to be zero (Eq. 5). The solution of Eqs. 3-5 allows us to calculate E_{ac} throughout the device, including the droplet.

Next we calculate the spatially resolved conductivity (σ) within the droplet by solving for distribution of ion concentration through Eqs. 6-8. The surface charge, σ_{OH} is calculated by assuming droplet $pH = 7$ and surface OH group density, $N_s \sim 10^{14}\ cm^{-2}$ [3]. Since the potential, V_{dc} due to surface charges (due to formation of double layer) is small ($< 0.1V$), the effective conductivity is essentially identical to that of bulk solution. Regardless, the approach described here is general and should apply to any biasing conditions. Note that the decoupling of the ac and dc Poisson equation (Eq. 2) is justified because the ac voltage V_{rms} $(22 - 36V) \gg V_{dc}$ $(< 0.1V)$.

Calculation of temperature distribution by thermal simulation:

The spatially resolved power dissipation (P) obtained from the numerical simulation of Poisson equation, is used to calculate the heat generation in the buffer solution (Eq. S10, S11) and the oxide (Eq. S10,S13). Time transient heat equation (Eq. S9) was solved using MATLAB® PDE toolbox [4] to determine the temporal and spatial heat profiles throughout the device. The heat generation terms include both Joule heating of ions in solution as well as dielectric relaxation in water and oxide, see Eqs. 11,13. Also, we assume that the electrical conductivity of the solution is proportional to the ionic concentration (Eq. S12). Convective transfer of heat from the droplet to the air was approximated by assuming that the droplet is covered by a $5\ \mu m$ thick boundary layer of air. Radiative heat transfer, however, was neglected in the simulation. The buffer solution and oxide are assumed to be free of any trap charges. The physical constants used in the simulation are listed in Supplementary Table 2, 4. Dirichlet boundary condition (Eq. S15) was applied on all the outer boundaries for the simulation and thermal fluxes were assumed to be continuous across the interfaces.

Discussion of the numerical results:

Supplementary Fig. S1 shows the electric field profile in the droplet obtained from the solution of Eq. (3) and Eq. (4). As expected, maximum electric field occurs near edges of the active device due to fringing effects. Consequently, the Joule heating of ions is maximum near the surface of the device. Also, as we increase the voltage (a-c), the fringing fields increase and hence, the temperature increases (Supplementary Fig. 1 a-c). The bottom panel in Fig. S1 a-c shows the temperature cut at the center of the device along the direction perpendicular to oxide surface.

Simulations for different droplet sizes (Supplementary Fig. S7), shows that the temperature becomes more uniform as the radius of the droplet decreases. Due to significant mismatch in thermal conductivity of the droplet vs. the substrate, we find that the maximum temperature is essentially independent of the droplet size, i.e ~ 4 degree change in temperature for 64 times increase in the volume of the droplet. This relative insensitivity of temperature to the droplet size allows precisely tuning of the droplet temperature regardless the inevitable variation in the droplet size.

Supplementary Methods:

Droplet evaporation:

To quantify droplet evaporation using the AC heating technique compared to a bulk heating technique, the diameter of droplets were measured before and after heating. Volume was calculated assuming a hemispherical shape of the droplet. AC Heating was accomplished by applying 30 V_{rms} for 2 minutes. This value corresponds to around 60°C in the core of the droplet. For the bulk heating, a stage heater from Instec Corporation was used to heat the chip and droplets to 60°C. Images were taken before and after heating and the diameter was measured using ImageJ.

Image capture and analysis:

To observe the changes in fluorescence, heating of the device took place on a Nikon Eclipse FN-1 fluorescence microscope stage. A B-2E/C FITC filter was used for monitoring the change in the fluorescein fluorescence. As the voltage was swept from 0-40V_{rms} at 2.4V_{rms} steps for 12 seconds each, a video was taken using NIS-Elements from Nikon, Inc. controlling a Nikon DS-Ri1 camera. These videos were then imported as a stack into NIH's software ImageJ. Each droplet's area was selected using oval selection. The mean grey value of the area selected through the entire stack was then measured. This provides a quantitative measurement of each individual droplet's fluorescence. This raw fluorescence was normalized and then plotted along with its derivative to provide the melting voltage for each droplet.

Supplementary Figure Legends

Supplementary Fig. S1: **Simulations of heating** (A) and (B) Plots of electric field and temperature for 22 V_{rms}. (C) and (D) Plots of electric field and temperature for 30 V_{rms}. (E) and (F) Plots of electric field and temperature for 36V_{rms}. (G) Thermal profile within the droplet at X = 0 μm for 20, 30 and 36 V_{rms}.

Supplementary Fig. S2: **AC vs. bulk heating evaporation** The AC heating technique shows a 2.5% average decrease in volume (n = 9, st. dev. 2.2%). The bulk heating technique shows a 16.7% average decrease in volume (n = 9, st. dev. 1.1%). The two-tailed P-value is < 0.0001.

Supplementary Fig. S3: **Fluorescent images of droplet fluorescence through a voltage sweep** (A), (B), and (C) show fluorescent images of the 50, 61 and 80°C FRET constructs, respectively, as the voltage is increased from 0-42V_{rms}. These images represent the data in Fig 4B.

Supplementary Fig. S4: **SYBR Green melting vs. FRET construct melting** A plot of the melting voltage vs. melting temperature plot with the FRET construct method and the SYBR green method. The melting voltages extracted from SYBR green melting fit the pattern established by the FRET construct melting points.

Supplementary Fig. S5: **Cross-sectional view of simulation schematic**

Supplementary Fig. S6: **Maximum temperature uniformity with varying droplet diameter** (A) 3 different diameter droplets were spotted on 3 linked devices. (B) Fluorescence increases uniformly with a voltage sweep. (C) The derivative of (B) is shown. The uniform peak for all 3 droplets implies a uniform maximum temperature in the droplets.

Supplementary Fig. S7: **Simulation of temperature profile uniformity in droplets of varying radius** Temperature becomes more uniform as the droplet radius becomes smaller.

Supplementary Fig. S8: **Uniform, parallel droplet heating** (A) Shows a bright field image of 5 droplets on linked devices where a single lead connects multiple heating elements. (B) A fluorescent image taken before the heating process. (C) A fluorescent image taken after heating of the 5 droplets simultaneously. The FRET construct has denatured resulting in an increase in observed fluorescence. (D) Raw fluorescence data taken during the voltage sweep. (E) A derivative of (D) provides the melting voltage for each droplet. The melting voltage is the same for all 5 devices which indicates uniform heating across the linked devices.

Supplementary Fig. S9: **Commercial data for the heteroduplex experiment** (A) and (B) show commercial melting curve and derivative data for the FRET constructs used in Fig. 4D and 4E. The heteroduplex shows a melting temperature 6-7℃ less than either of the fully complementary strands.

Supplementary Fig. S10: **FRET construct dehydration and rehydration** (A) A schematic of the dehydration/rehydration process. A probe ssDNA sequence is dried on the device surface. The probe ssDNA is rehydrated using low evaporation solution containing the target ssDNA

sequence. (B) and (C) The melting curve and derivative of the initial heating-cooling step. The fluorescence increases in dual-peak manner, implying improper initial DNA hybridization.

Supplementary Fig. S11: **Dehydration/rehydration of dsDNA FRET construct** (A) Pictures of the process flow are presented. (i) Shows bare device. (ii) dsDNA FRET construct is dehydrated on the surface. (iii) A fluorescence image of the spotted dsDNA. (iv) 3 of the dsDNA spots are rehydrated with the low evaporation Protein Carrier Solution. (v) A fluorescence image of the rehydrated dsDNA. (B) & (C) A melting curve of the rehydrated dsDNA is taken. The fluroescence shows a single distinct peak implying proper DNA hybridization and melting.

Supplementary Table S1: **Description of symbols**

Supplementary Table S2: **Parameters for electrostatics simulation** (Refer to Eqs. (1-8) in Supplementary Table S3)

Supplementary Table S3: **Summary of model equations** (Refer to Supplementary Table 1, 2, and 4 and Supplementary Figure S5)

Supplementary Table S4: **Thermal simulation parameters** (Refer to Eqs. (9-15) in Supplementary Table S3)

Supplementary Table S5: **Averages and standard deviations from Fig. 1** Multiple single droplet denaturation studies were completed using the 50, 61 and 80℃ FRET constructs.

Supplementary Table S6: **Sequence, melting temperature and melting voltage for the dsDNA fragments used in the SYBR Green denaturation experiment from Supplementary Fig. S6**.

Supplementary Table S7: **Averages and standard deviations from Fig. 4B and 4C.** Multiple parallel droplet denaturation studies were completed using the 50, 61 and 80℃ FRET constructs.

Supplementary Table S8: **Averages and standard deviations from Fig. 4D and 4E**. Multiple parallel droplet denaturation studies were completed using the 71.7, 70.2, and Heteroduplex of 71.7 and 70.4º FRET constructs.

Supplementary Figure S1

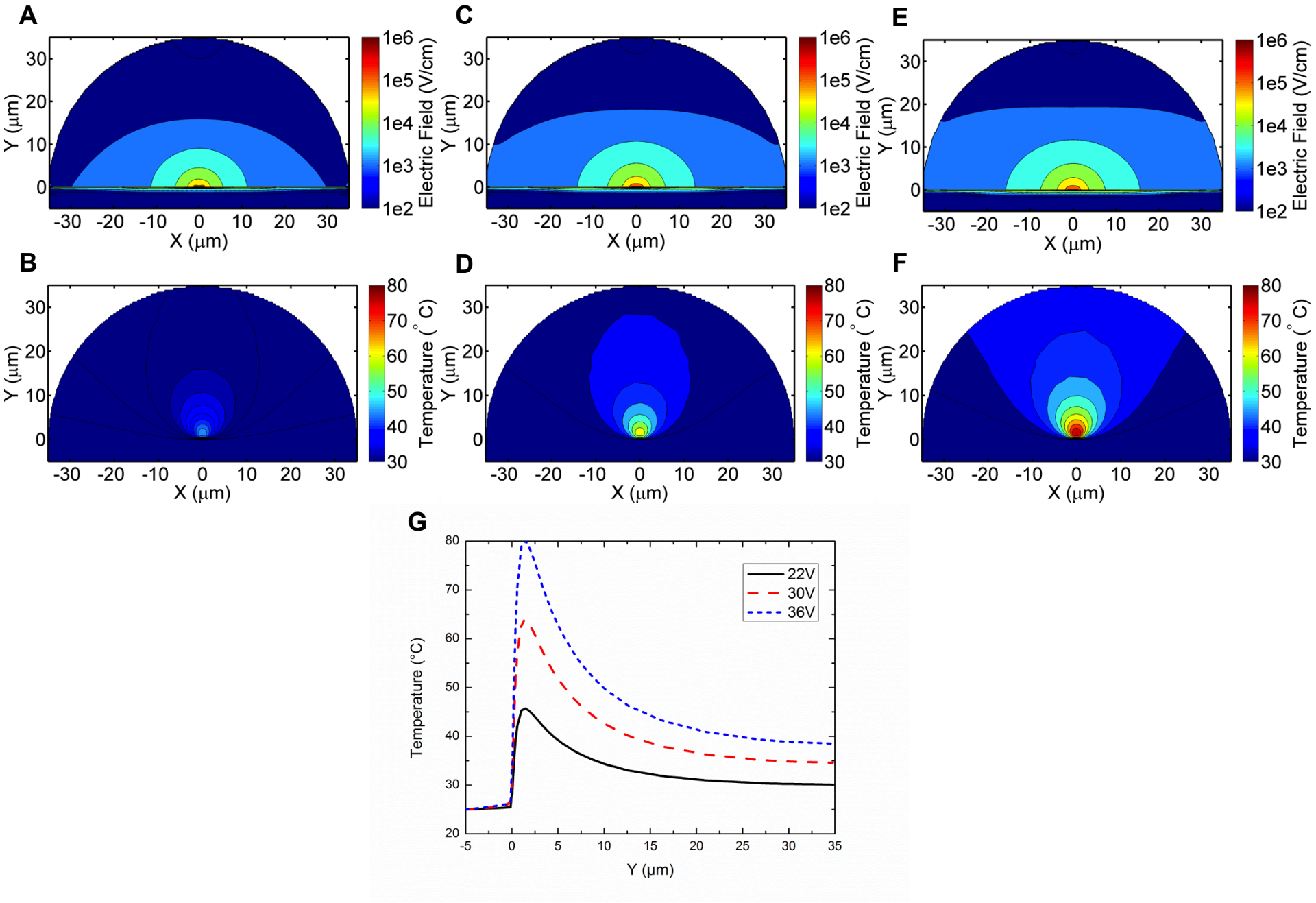

Supplementary Figure S2

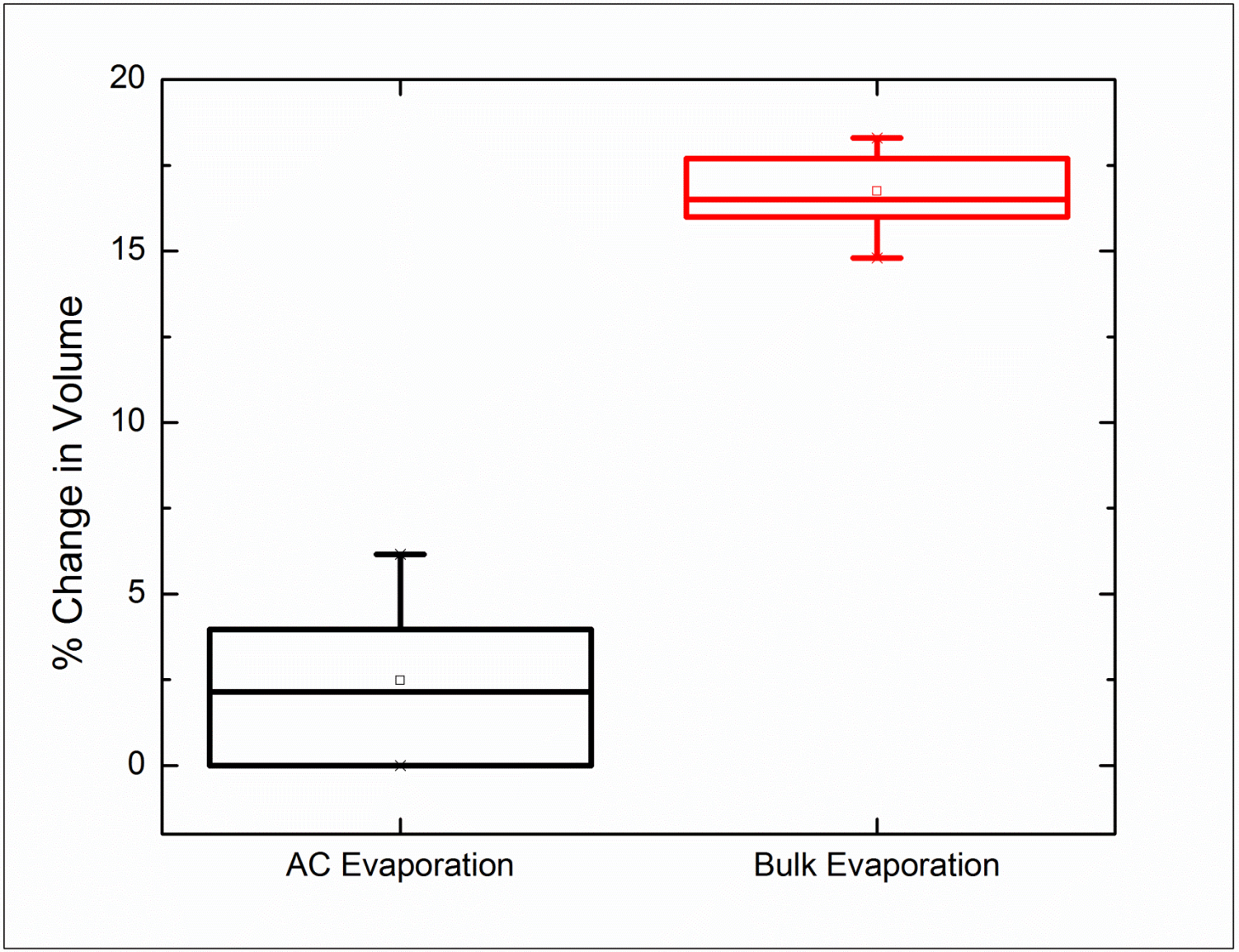

Supplementary Figure S3

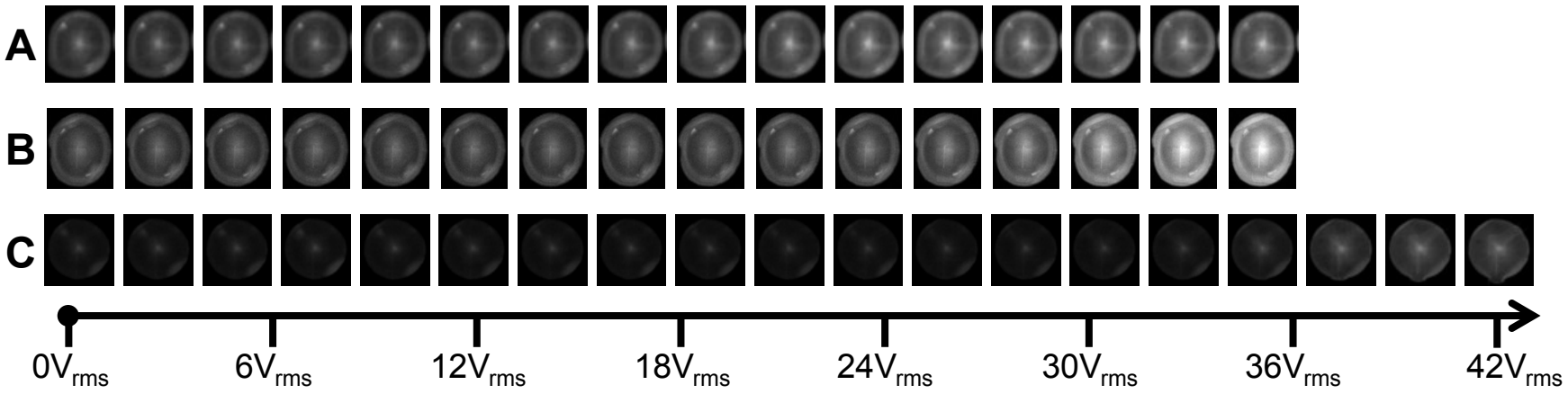

Supplementary Figure S4

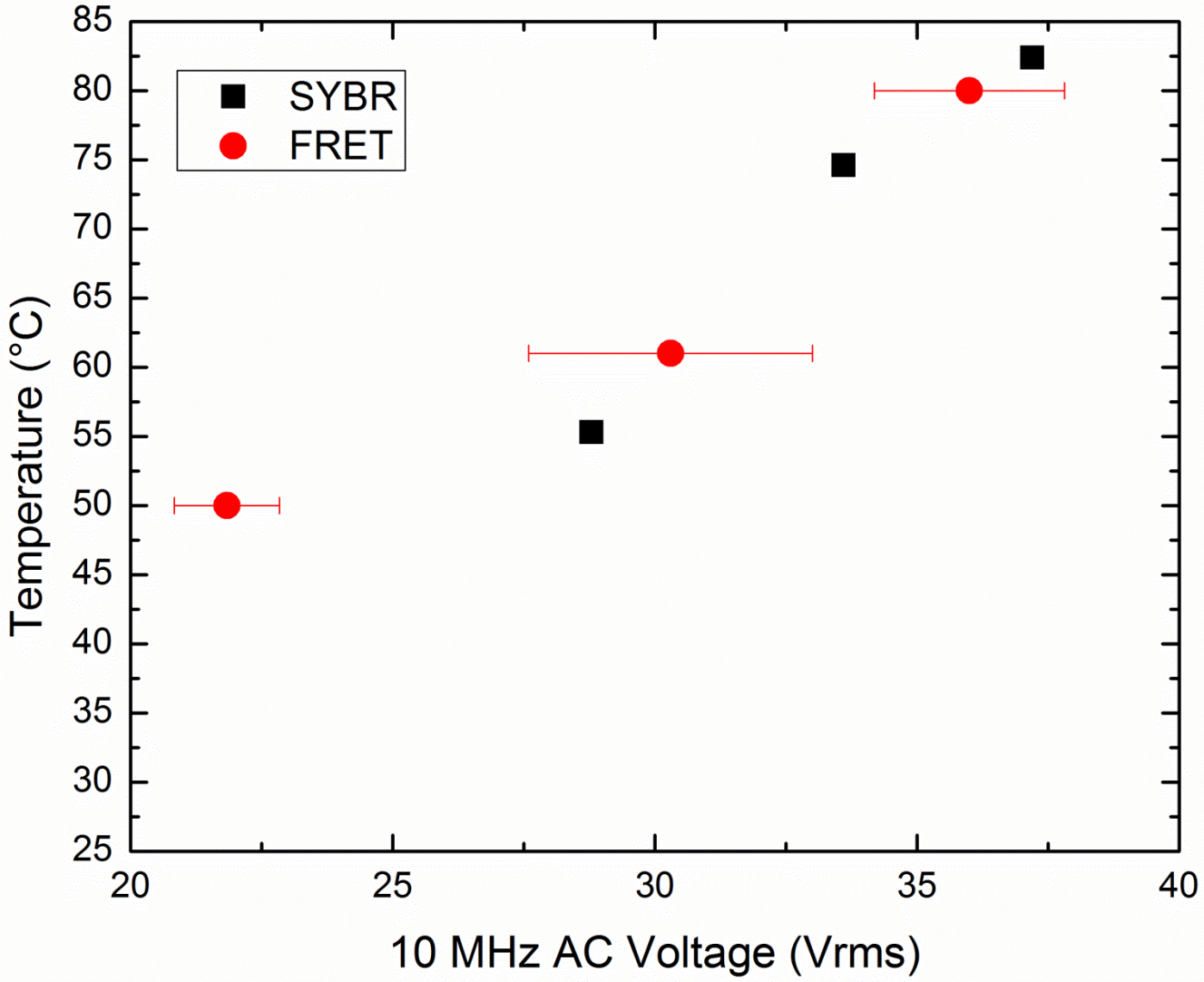

Supplementary Figure S5

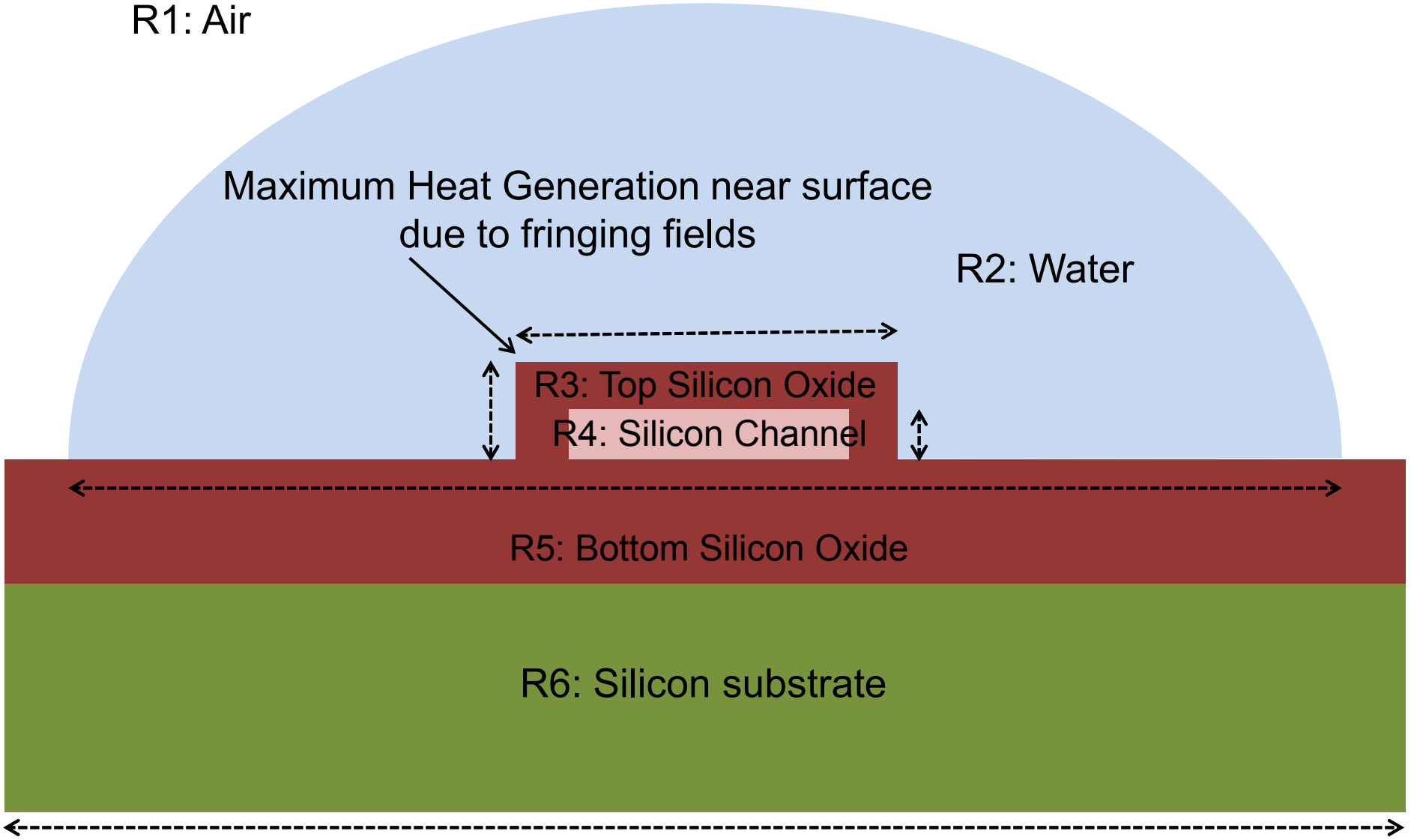

Supplementary Figure S6

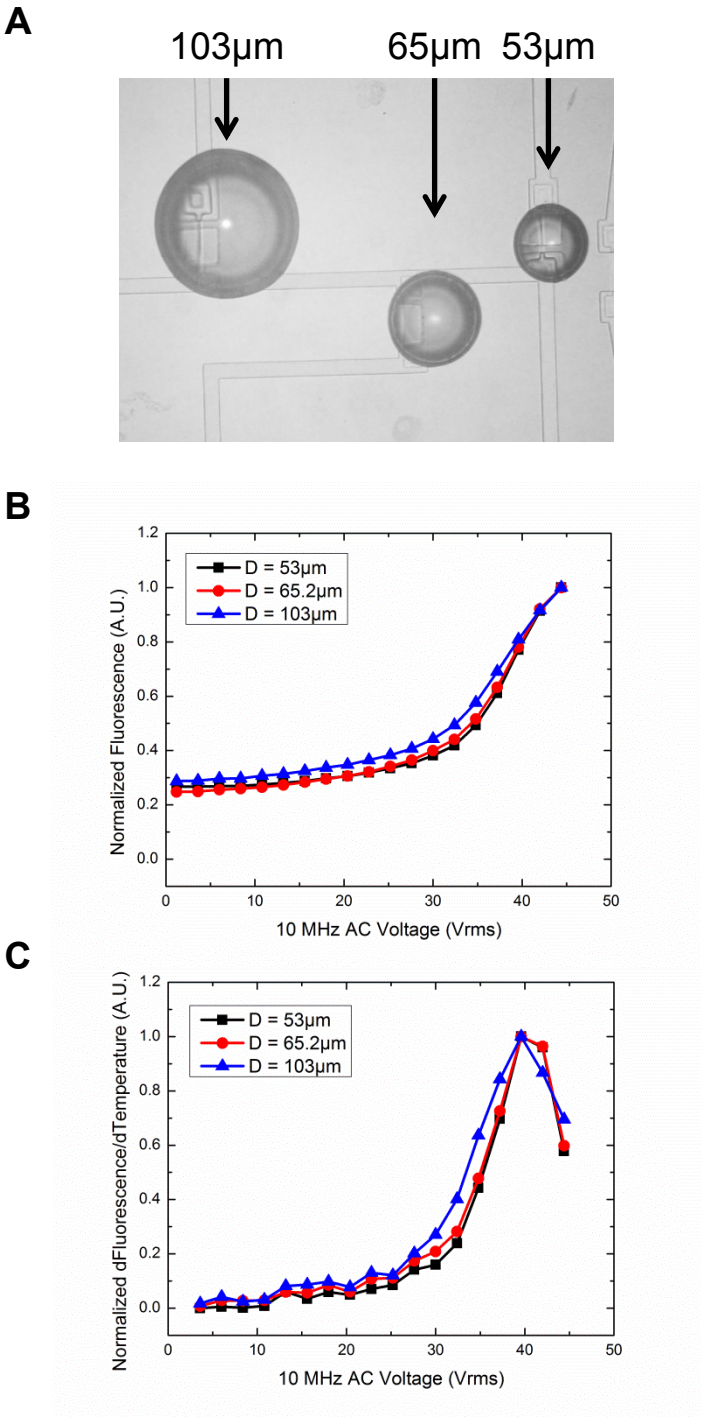

Supplementary Figure S7

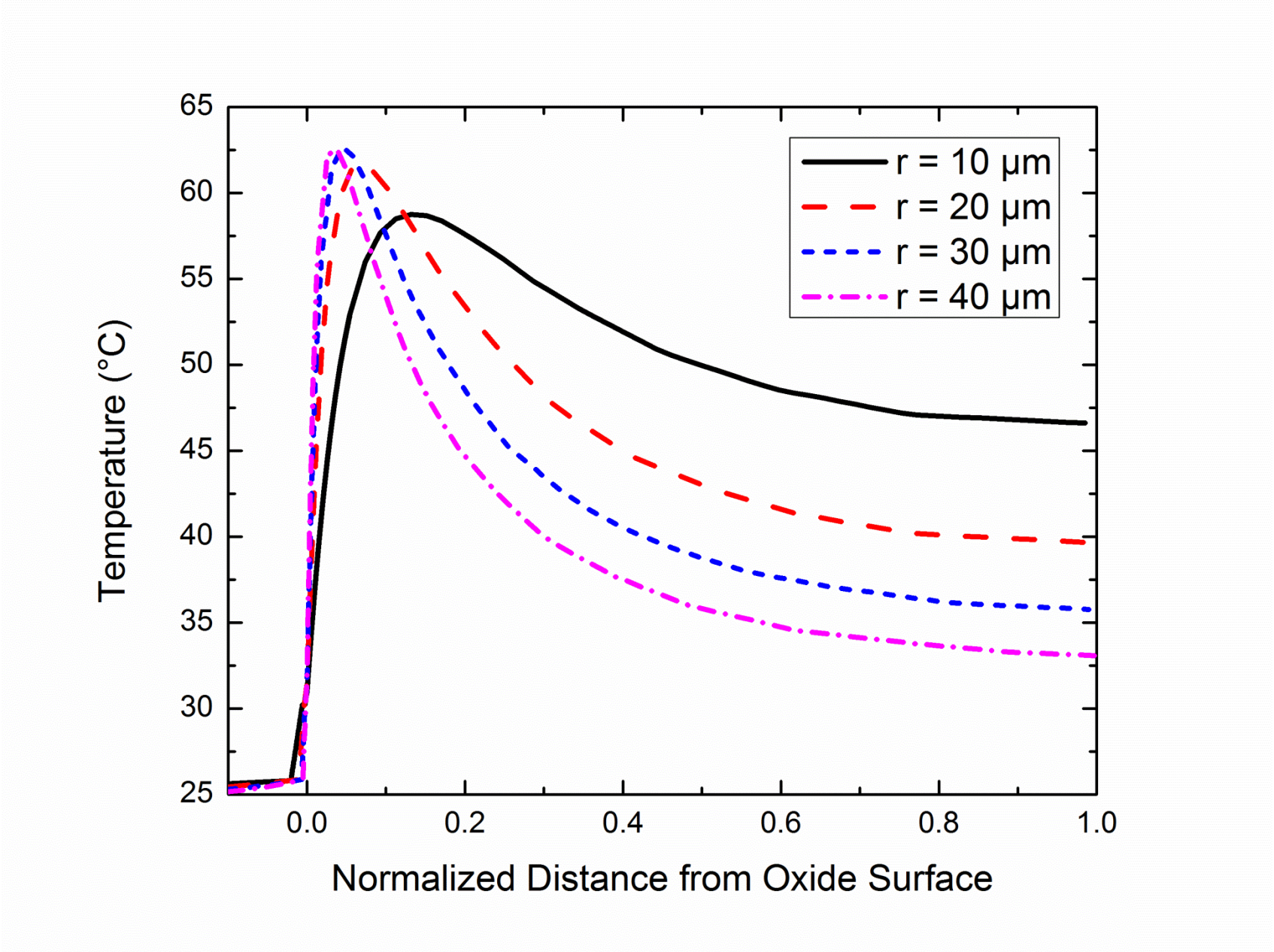

Supplementary Figure S8

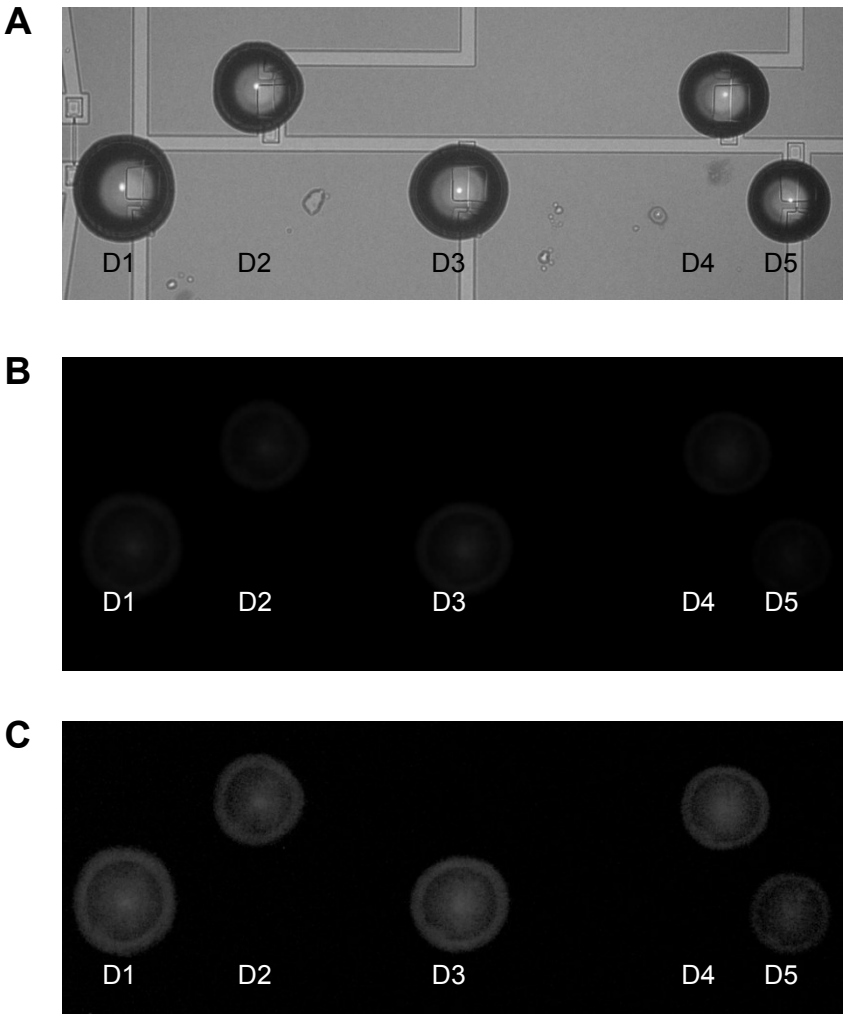

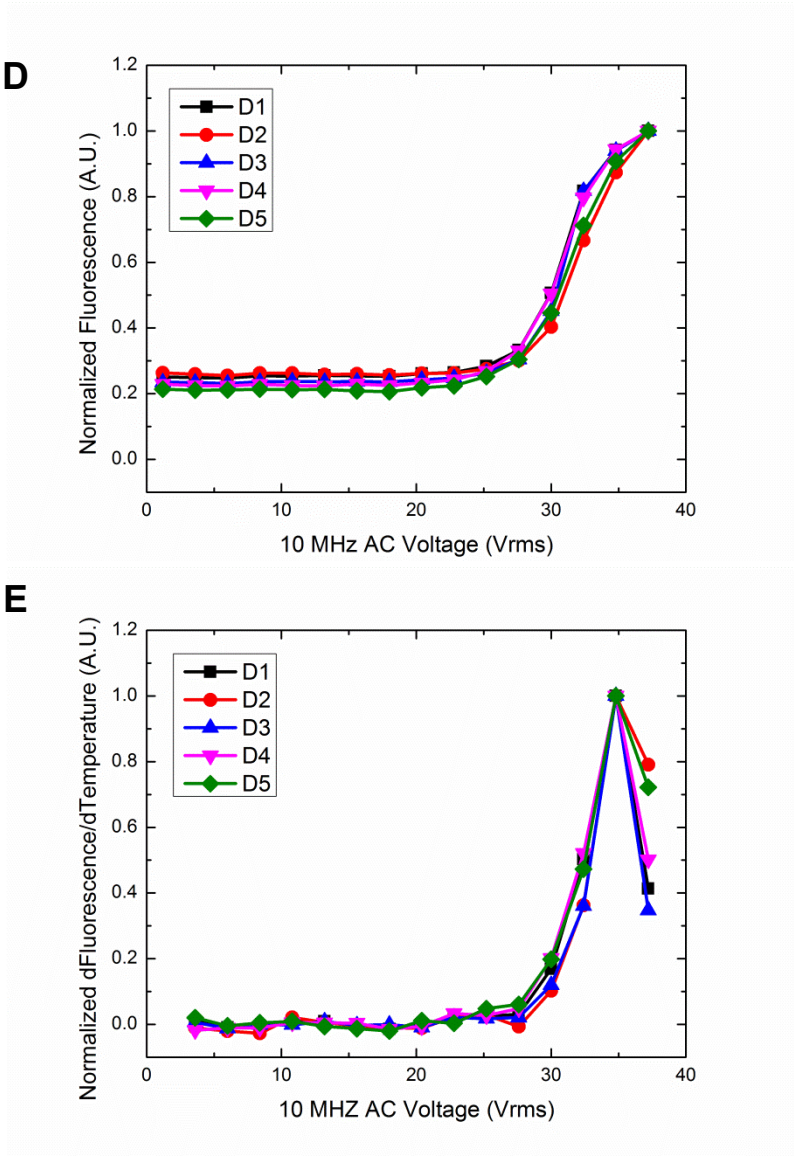

Supplementary Figure S9

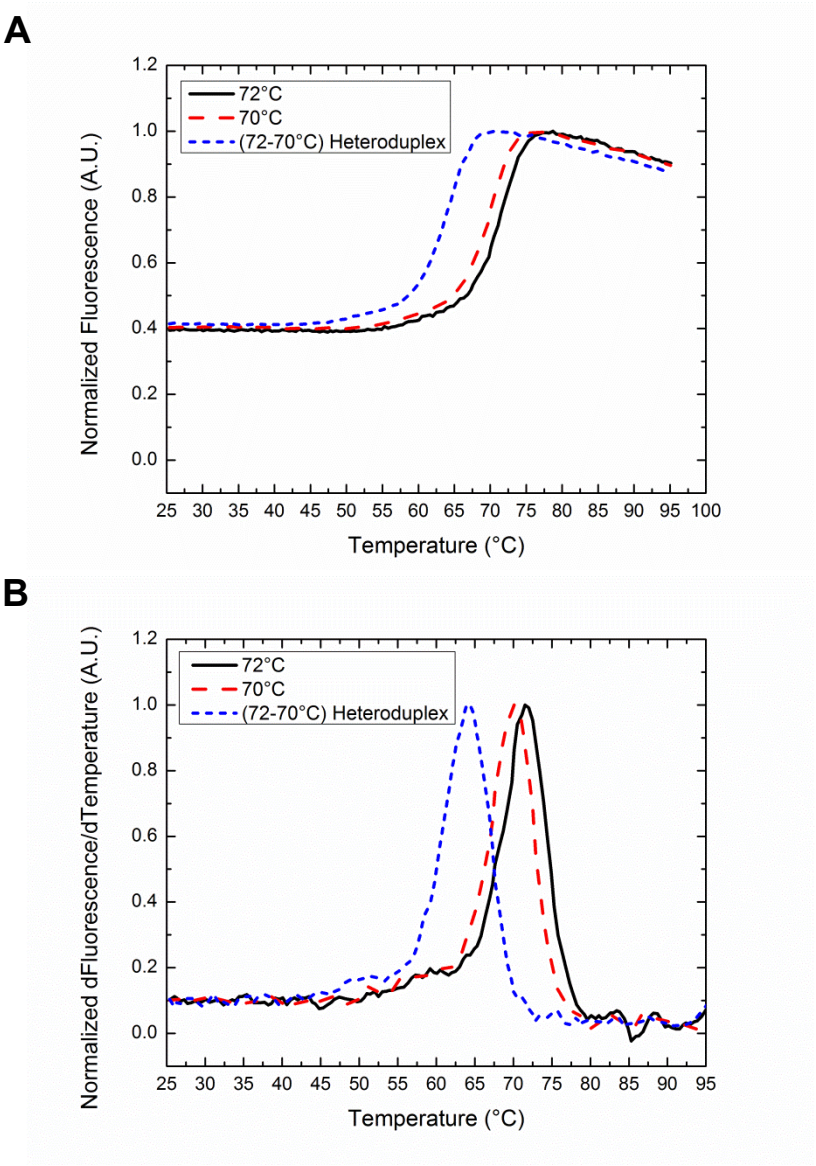

Supplementary Figure S10

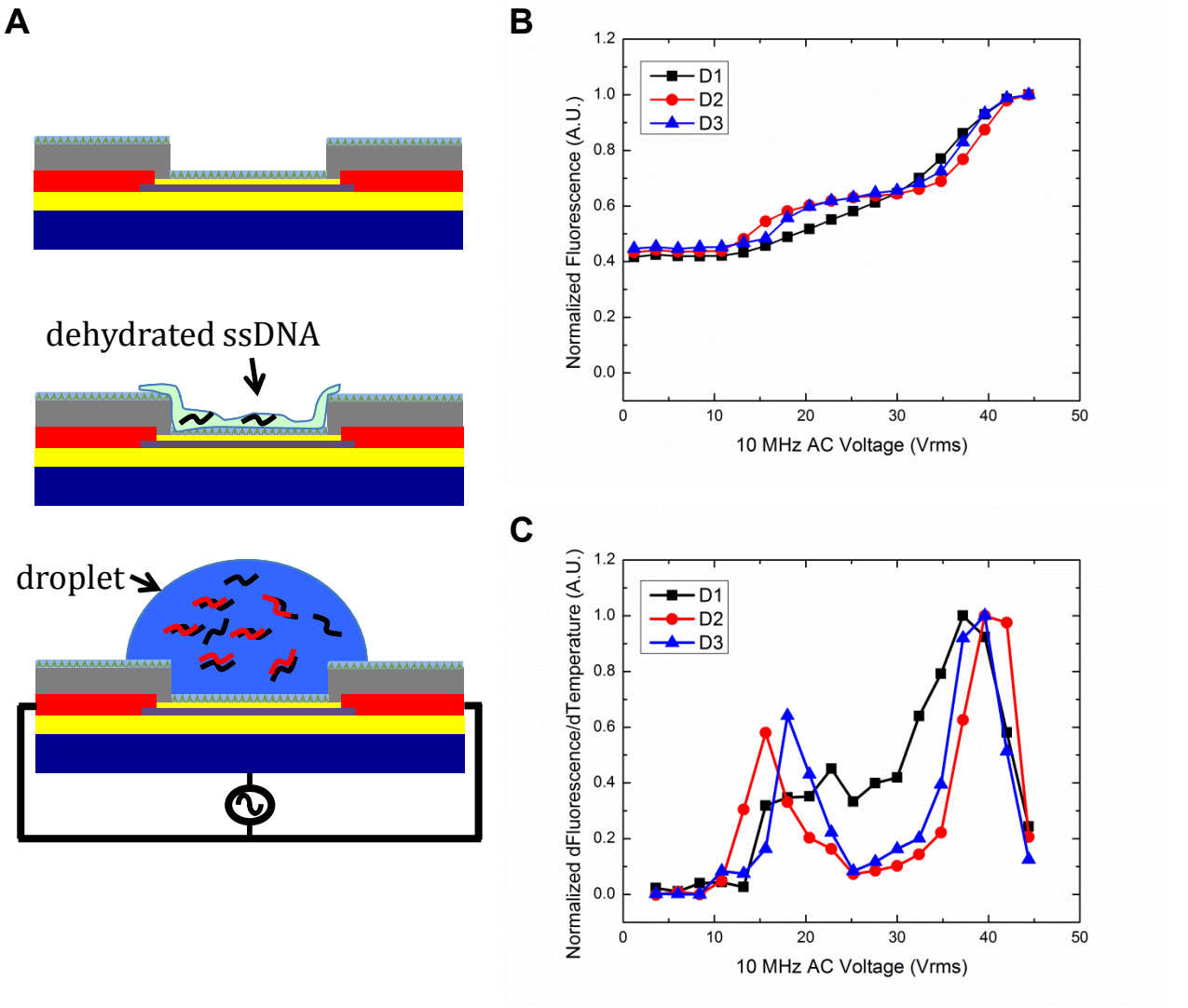

Supplementary Figure S11

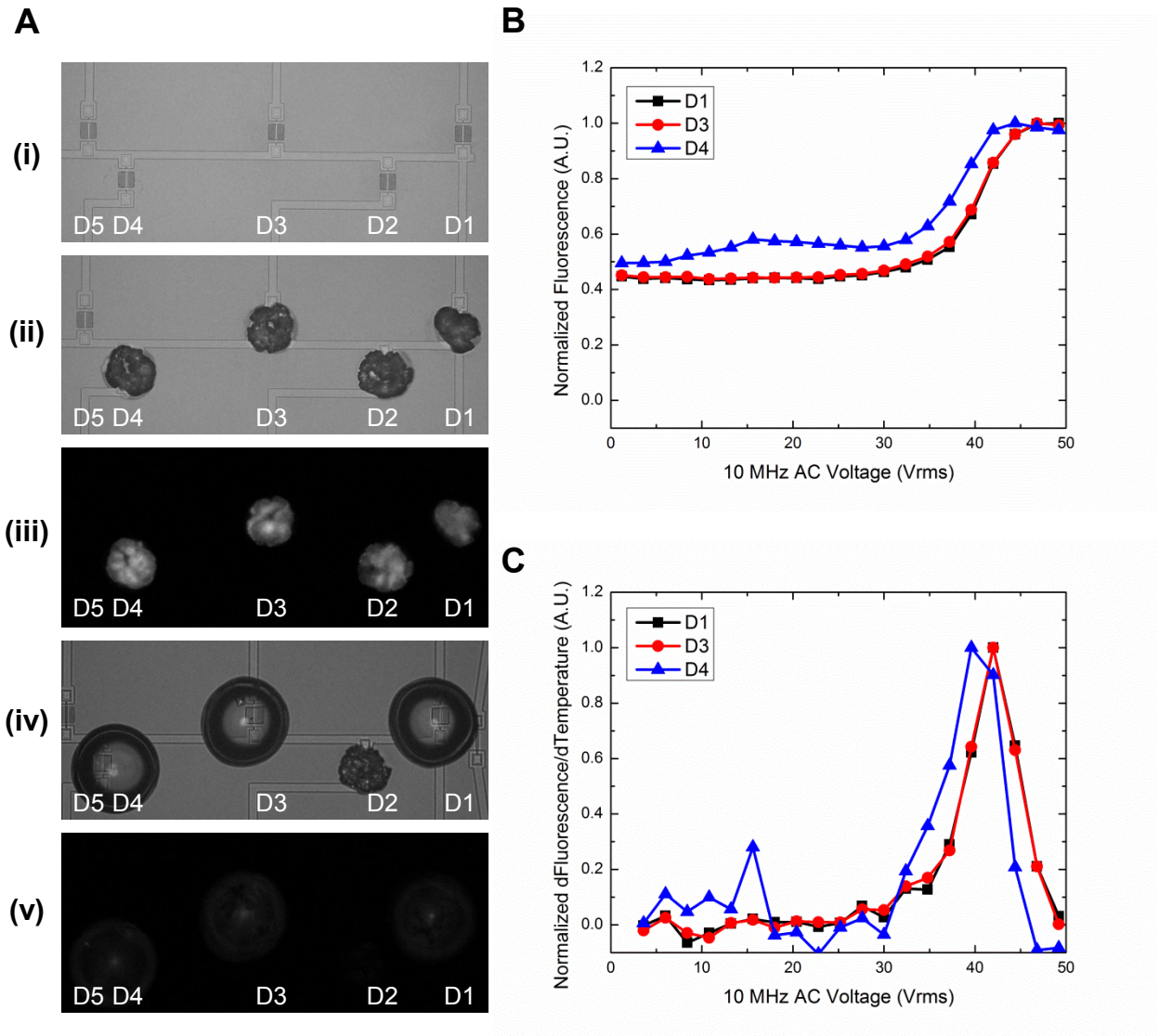

Supplementary Table 1

Symbol	Description
ϕ	Net potential
ϕ_{ac}	Potential due to applied ac bias
ϕ_{dc}	Potential due to surface charges
ρ	Density of charges
ϕ_{ch}	Channel potential
ϕ_{bulk}	Potential at the bulk contact
V_{BG}	Applied ac bias
σ_{OH}	Surface charge due to ionization of Silanol (*SiOH*) groups
ρ_{ion}	Ionic charge in droplet
T	Temperature
t	Time
σ	Conductivity in the specified region
σ_{ion}	Conductivity due to *NaCl*
E_{ac}	Field obtained from ac simulation
T_b	Temperature at all outer boundaries

Supplementary Table 2

Parameter	Symbol	Numerical value/units	Ref
Permittivity in Free Space	ϵ_0	$8.85*10^{-12}$ F/m	[5]
Relative Permittivity in Air	ϵ_a	1	-
Relative Permittivity in Water	ϵ_w	78.8	[7]
Relative Permittivity in oxide	ϵ_{ox}	3.9	[8]
Relative Permittivity in silicon	ϵ_{Si}	11.8	[9]
Electronic Charge	q	$1.6*10^{-19}$ C	[5]
Boltzmann Constant	k_B	$1.38*10^{-23}m^2kgs^{-2}$	[5]

Supplementary Table 3

Equations for electrostatics:			**Ref**
$-\nabla.(\epsilon\nabla\phi) = \rho$		(1)	[5]
$\phi = \phi_{ac} + \phi_{dc}$		(2)	
AC Simulations (for obtaining the electric field profile):			
$\nabla.(\epsilon\nabla\phi_{ac}) = 0$	(Region: R2-R6)	(3)	
$E_{ac} = -\nabla\phi_{ac}$		(4)	
Boundary Conditions: $\phi_{ch} = 0;\ \phi_{bulk} = V_{BG}$		(5)	
DC Simulations (for obtaining the conductivity):			
$-\nabla.(\epsilon\nabla\phi_{dc}) = \rho_{ion}$		(6)	
$\rho_{ion} = 2qn_0 \sinh\left(\frac{q\phi_{dc}}{k_B T}\right)$	(Region: R2)	(7)	
Boundary Condition: $-\epsilon_w\nabla\phi_{dc} = \sigma_{OH}$	(Region: R2-R3, R2-R5 interface)	(8)	[6]

Equations for Thermal conduction:			
$\rho C\frac{\partial T}{\partial t} = \nabla.(\kappa\nabla T) + P$		(9)	
$P = \frac{1}{2}\sigma E_{ac}^2$		(10)	
$\sigma = \epsilon_w''\epsilon_0\omega + \sigma_{ion}$	(Region: R2)	(11)	[7]
$\sigma_{ion} = \rho_{ion}\alpha(\lambda_{Na^+} + \lambda_{Cl^-})$		(12)	
$\sigma = \epsilon_{ox}''\epsilon_0\omega$	(Region: R3, R5)	(13)	[5]
$\sigma = 0$	(Region: R1,R4,R6)	(14)	
Boundary Conditions: $T_b = 298K$ (Temperature at all outer boundaries)		(15)	

Supplementary Table 4

Parameter	Symbol	Numerical value/units	Ref
Thermal conductivity of Air	k_a	*0.024 W/m.K*	[10]
Thermal conductivity of Water	k_w	*0.58 W/m.K*	[11]
Thermal conductivity of oxide	k_{ox}	*1.4 W/m.K*	[12]
Thermal conductivity of silicon	k_{si}	*149 W/m.K*	[12]
Mass density of air	ρ_a	*1.2 kg/m^3*	[10]
Mass density of water	ρ_w	*1000 kg/m^3*	[12]
Mass density of oxide	ρ_{ox}	*2600 kg/m^3*	[12]
Mass density of silicon	ρ_{si}	*2300 kg/m^3*	[12]
Specific Heat Capacity of air	C_a	*1000 J/kg.K*	[10]
Specific Heat Capacity of water	C_w	*4180 J/kg.K*	[13]
Specific Heat Capacity of oxide	C_{ox}	*1000 J/kg.K*	[12]
Specific Heat Capacity of silicon	C_{si}	*710 J/kg.K*	[12]
Loss factor in oxide at *10 MHz*	$\epsilon_{ox''}$	*3.9*10^{-4}*	[5]
Loss factor in water at *10 MHz*	$\epsilon_{w''}$	*0.1*	[7]
Limiting Molar conductivity of Na^+	λ_{Na+}	*50 Scm^2/mol*	[14]
Limiting Molar conductivity of Cl^-	λ_{Cl-}	*76 Scm^2/mol*	[14]
Surface Silanol (SiOH) group density	N_s	*5*10^{14} cm^{-2}*	[3]
Ionic concentration of *NaCl*	n_0	*225 mM*	-
pH of buffer solution	*pH*	7	-
Frequency	$\omega/2\pi$	*10 MHz*	-
Calibration parameter	α	0.20	-

Supplementary Table 5

FRET construct with melting temperature	Average melting voltage	Standard deviation
(1) 50°C	21.84	1.00 (n=5)
(2) 61°C	30.3	2.70 (n=8)
(3) 80°C	36.0	1.81 (n=8)

Supplementary Table 6

	Sequence	Measured melting temperature (T_m)	Measured melting voltage (V_m)
1	5’-AGGCTTAGCTACA-3’ 3’-TCCGAATCGATGT-5’	55°C	28.8 V_{rms}
2	5’-CGCACCCAGGCTTAGCTACAAACAT-3’ 3’-GCGTGGGTCCGAATCGATGTTTGTA-5’	75°C	33.6 V_{rms}
3	5’-CGCACCCAGGCTTAGCTACAAACCGTCACTGGCATTGCAGTT-3’ 3’-GCGTGGGTCCGAATCGATGTTTGGCAGTGACCGTAACGTCAA-5’	82°C	37.2 V_{rms}

Supplementary Table 7

FRET construct with melting temperature	Average melting voltage	Standard deviation
(1) 50°C	17.04	1.31 (n=5)
(2) 61°C	26.16	2.15 (n=5)
(3) 80°C	33.36	1.31 (n=5)

Supplementary Table 8

FRET construct with melting temperature	Average melting voltage	Standard deviation
(4) 71.7°C	35.76	3.64 (n=5)
(5) 70.2°C	35.76	2.15 (n=5)
(4-5) Heteroduplex 64.1°C	28.08	1.07 (n=5)

References:

[1] "Sentaurus Device." [Online]. Available: http://www.synopsys.com/tools/tcad/devicesimulation/pages/sentaurusdevice.aspx.

[2] T. M. Squires and M. Z. Bazant, "Induced-charge electro-osmosis," *Journal of Fluid Mechanics*, vol. 509, pp. 217-252, Jun. 2004.

[3] P. Bergveld, "A general model to describe the electrostatic potential at electrolyte oxide interfaces," *Advances in Colloid and Interface Science*, vol. 69, pp. 31-62, 1996.

[4] "MATLAB PDE Toolbox." [Online]. Available: http://www.mathworks.com/products/pde/.

[5] S. Ramo, J. R. Whinnery, and T. V. Duzer, *Fields and Waves in Communication Electronics*, vol. 2. Wiley, 1994, p. 864.

[6] P. Bergveld, R. E. G. V. Hal, and J. C. T. Eijkel, "The remarkable similarity between the acid-base properties of ISFETs and proteins and the consequences for the design of ISFET biosensors," *October*, vol. 10, pp. 405-414, 1995.

[7] C. Gabriel, S. Gabriel, E. H. Grant, S. J. Halstead, D. P. Michael, and B. S. J. Halstead, "Dielectric parameters relevant to microwave dielectric heating," vol. 27, pp. 213-223, 1998.

[8] R. F. Pierret, "Advanced Semiconductor Fundamentals Second Edition," *Computer Engineering*, p. 221, 2002.

[9] R. Hull, *Properties of crystalline silicon*. IET, 1999, p. xxvi+1016.

[10] R. B. Montgomery, "Viscosity and thermal conductivity of air and diffusivity of water vapor in air," *Journal of Meteorology*, vol. 4, no. 6, pp. 193-196, Dec. 1947.

[11] M. L. V. Ramires, C. a. Nieto de Castro, Y. Nagasaka, A. Nagashima, M. J. Assael, and W. a. Wakeham, "Standard Reference Data for the Thermal Conductivity of Water," *Journal of Physical and Chemical Reference Data*, vol. 24, no. 3, p. 1377, 1995.

[12] J. L. N. S. Sang-Joon, *Microfabrication for Microfluidics*. Artech house, 2010.

[13] D. R. Kimbrough, "Heat Capacity, Body Temperature, and Hypothermia," *Journal of Chemical Education*, vol. 75, no. 1, p. 48, Jan. 1998.

[14] L. Coury and D. Ph, "Conductance Measurements Part 1 : Theory," *Current Separations*, vol. 3, no. 2, 1999.